Bioprinting 21 (2021) e00125

Contents lists available at ScienceDirect

Bioprinting

journal homepage: www.elsevier.com/locate/bprint

Continuous chaotic bioprinting of skeletal muscle-like constructs

Edna Johana Bolívar-Monsalve [a,1], Carlos Fernando Ceballos-González [a,1], Karen Ixchel Borrayo-Montaño [a], Diego Alonso Quevedo-Moreno [b], Juan Felipe Yee-de León [c], Ali Khademhosseini [d], Paul S. Weiss [d,e,f,g,h], Mario Moisés Alvarez [a,i,**], Grissel Trujillo-de Santiago [a,b,*]

[a] Centro de Biotecnología-FEMSA, Tecnologico de Monterrey, Monterrey, NL, 64849, Mexico
[b] Departamento de Ingeniería Mecatrónica y Eléctrica, Escuela de Ingeniería y Ciencias, Tecnologico de Monterrey, Monterrey, NL, 64849, Mexico
[c] Delee Corp., Mountain View, CA, 94041, USA
[d] Terasaki Institute for Biomedical Innovation, Los Angeles, CA, 90024, USA
[e] Department of Chemistry and Biochemistry, University of California, Los Angeles, Los Angeles, CA, 90095, USA
[f] Department of Bioengineering, University of California, Los Angeles, Los Angeles, CA, 90095, USA
[g] Department of Materials Science and Engineering, University of California, Los Angeles, Los Angeles, CA, 90095, USA
[h] California NanoSystems Institute (CNSI), University of California, Los Angeles, Los Angeles, CA, 90095, USA
[i] Departamento de Bioingeniería, Escuela de Ingeniería y Ciencias, Tecnologico de Monterrey, Monterrey, NL, 64849, Mexico

ARTICLE INFO

Keywords:
Bioprinting
Kenics
Skeletal muscle
Chaotic
Cell alignment

ABSTRACT

In this study, chaotic flows are used to biofabricate muscle tissue-like constructs that mimics the hierarchical architecture of native skeletal muscle. Multi-layered and multi-material filaments (~1.2 mm in diameter) are easily obtained in a one-step extrusion protocol by using a Kenics static mixer (KSM). These filaments contain intercalated layers (~130 μm in thickness) of myoblast-laden gelatin-methacryloyl (GelMA)-alginate and physical barriers composed of alginate. Cells exhibit a high post-printing viability (>85%) and remain highly viable even at 28 days after bioprinting. Alginate barriers prevent cells from migrating to neighboring layers. The spatially controlled microarchitecture achieved here, resembles a muscle fascicle at each intercalated layer. This straightforward approach promotes an effective alignment of cells (~60%) with respect to the filament axis. The expression of myosin and sarcomeric actin was verified at day 28. In summary, we demonstrate the fabrication of a hierarchically structured engineered muscle-like constructs in a continuous and simple fashion using an extrusion-based technique that modulates printing resolution simply by switching the number of KSM elements in the printhead.

1. Introduction

Nature is an exceptional factory of living systems composed of extraordinary hierarchical structures. Remarkable examples are the beautiful layers inside bamboo trees [1], the concentric multilayered structures that make up a dragonflies' wings [2], and the networks of spicules that protect and bring support to 'glass' sponges [3]. The human body is no exception, as the highly organized microstructures found in bones [4], tendons [5], and even in our brains [6] demonstrate that human tissues also display hierarchical architectures on which complex physiological functions depend.

In skeletal muscles, the muscle fascicle is the largest structural block (Fig. 1A) and is represented by a bundle of myotubes (also known as muscle fibers), capillaries, and nerves. Each myotube contains multiple myofibrils approximately 2 μm diameter that are formed by packed protein arrays called sarcomeres [7]. In this hierarchical architecture, the sarcomere, which is composed of myosin and sarcomeric actin proteins, is the nano-structured functional unit responsible for skeletal muscle contraction [8,9]. The spatial orientation of these proteins within the sarcomere is what dictates muscle contractile functionality [10]; therefore, the muscle must be delicately and diligently assembled to ensure unidirectional alignment of the myotubes for the effective contraction of sarcomeres [11,12].

* Corresponding author. Centro de Biotecnología-FEMSA, Tecnologico de Monterrey, Monterrey, NL, 64849, Mexico.
**Corresponding author. Centro de Biotecnología-FEMSA, Tecnologico de Monterrey, Monterrey, NL, 64849, Mexico.
E-mail addresses: mario.alvarez@tec.mx (M.M. Alvarez), grissel@tec.mx (G. Trujillo-de Santiago).
[1] Authors contributed equally to this work.

https://doi.org/10.1016/j.bprint.2020.e00125
Received 22 August 2020; Received in revised form 23 December 2020; Accepted 23 December 2020

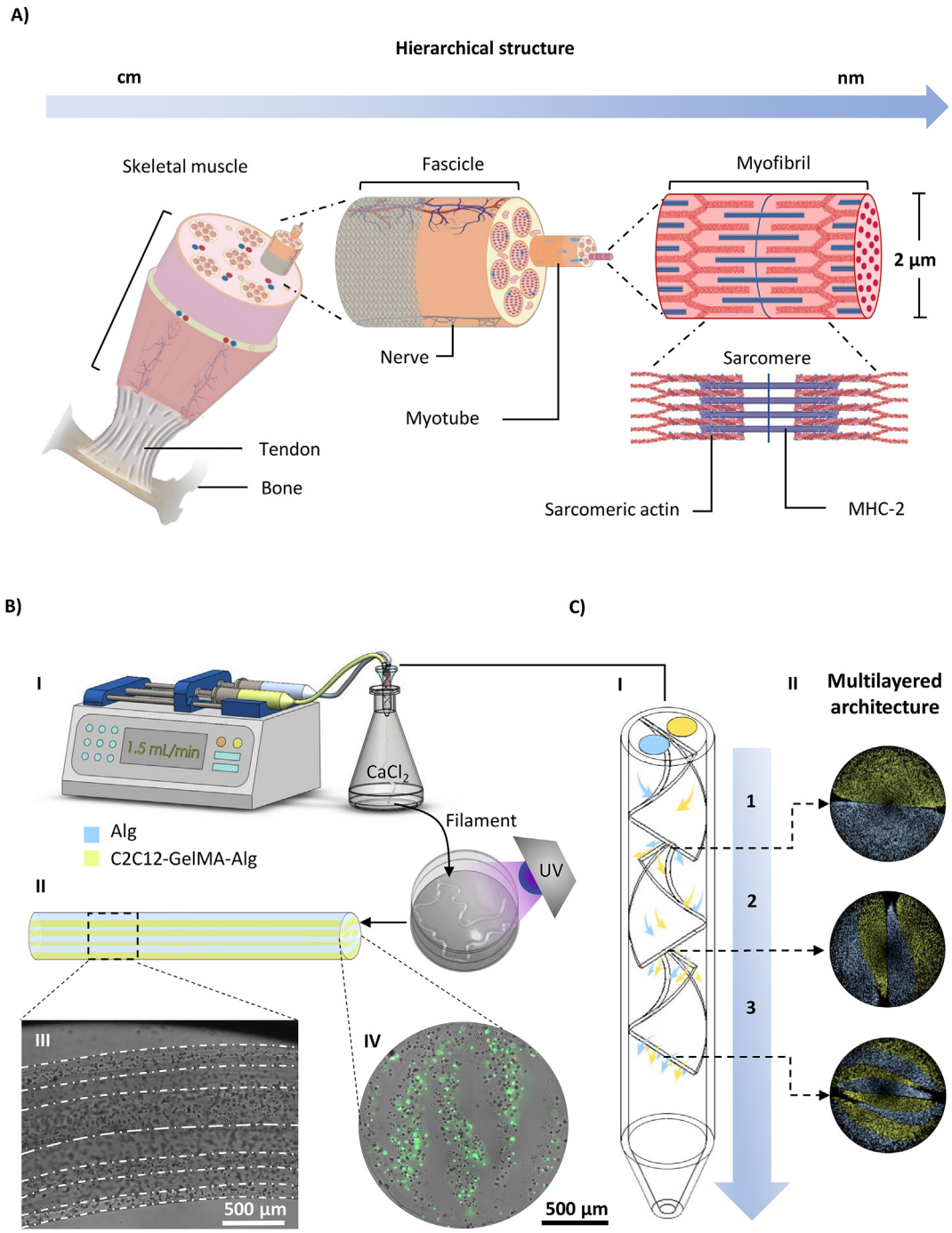

Fig. 1. Chaotic bioprinting of a microstructured muscle model. **A)** Illustration showing the hierarchical organization of the skeletal muscle. The largest structural blocks in this tissue are the muscle fascicles, *i.e.*, bundles of myotubes. Each of these multinucleated cells contains high-aspect-ratio myofibrils composed of sarcomeres, *i.e.*, the protein assemblies responsible for muscle contraction. **B)** Schematics of the bioprinting setup implemented for **(I)** coextrusion of a myoblast (C2C12)-laden bioink, along with a pristine alginate ink, using a printhead containing three Kenics static mixer (KSM) elements. **(II)** Illustration of a chaotically printed filament exhibiting inner layers. Representative bright-field and fluorescence micrographs showing the **(III)** cross-sectional and **(IV)** axial view of printed constructs with several viable C2C12 cells at day 1, and preservation of multilayered architecture, respectively. **C)** Computational simulation results of a chaotic printing process. **(I)** Successive stretching and folding of two materials (represented in blue and yellow) extruded through a KSM printhead. Each fluid is bifurcated and reoriented by each KSM element, generating an exponential increase in the number of flow streams. **(II)** The cross-section of the multilayered structure developed after each KSM element.

In tissue engineering, this assembly process has been mimicked by approaches that include self-assembly [13,14], micromolding [11,15, 16], photo-patterning [17], and 3D-bioprinting [18–21]. After establishment of the general structure, further cell orientation and alignment is typically promoted or enhanced through physical and chemical stimulation [10,22,23]. Among muscle biofabrication strategies, extrusion-based bioprinting is one of the most popular due to its relative simplicity and inexpensive equipment requirements. However, even in the best case scenario, the resolution of extrusion bioprinters is ~200 µm [20,24,25], which makes unidirectional accommodation of skeletal muscle cells difficult to achieve [26].

We recently introduced the concept of continuous chaotic

bioprinting, a straightforward extrusion technique that uses chaotic advection to create living microsystems composed of mammalian or bacterial cells at a resolution as small as 10 μm [27]. Chaotic printing uses chaotic flows to produce highly aligned microstructures in a fast, reproducible, and predictable fashion that is amenable to mathematical modeling [28–30]. Based on our previous work, here we have printed, in a single step, a biomimetic muscle model that exhibits a hierarchical structure of highly aligned myotubes containing myofibrils displaying a narrow distribution orientation.

2. Materials and methods

2.1. Cell culture

Mouse myoblasts (C2C12 cell line, ATCC) were expanded in Dulbecco's modified Eagle medium/high glucose (CAS 9005-38-3, Sigma-Aldrich, St. Louis, MO, USA), supplemented with 10% fetal bovine serum (Gibco) by culture at 37 °C in a humidified 5% CO_2 atmosphere.

2.2. Synthesis of GelMA

GelMA exhibiting a high degree of methacrylation was prepared based on a previously developed protocol with slight modifications [31]. Briefly, 10% (w/v) type A porcine skin gelatin (Sigma-Aldrich, USA) was dissolved in Dulbecco's phosphate-buffered saline (DPBS) under stirring at 350 rpm and 50 °C. Subsequently, 20% v/v methacrylic anhydride (MA) (Sigma-Aldrich, USA) was added dropwise to the solution at 0.5 mL/min with a peristaltic pump. After a 1 h reaction, four volumes of DPBS were added to the solution, and unreacted MA was removed by dialysis against deionized water at 40 °C for 1 week until of the solution reached pH 7.4. The solution was then frozen at −80 °C and freeze-dried for 4 days. The lyophilized GelMA was stored at −80 °C for further use.

2.3. Preparation of hydrogels

We prepared hydrogel solutions composed of GelMA (3% and 5% w/v), alginate (1%, 2%, and 4% w/v) (Sigma-Aldrich, St. Louis, MO, USA), and 3% GelMA and 1% alginate. The polymers were dissolved in DPBS. GelMA-containing hydrogels were also mixed with 0.067% lithium phenyl-2,4,6-trimethylbenzoylphosphinate (LAP) and heated at 70 °C for 15 min. Solutions were tempered at 40 °C for rheological analyses.

2.4. Rheological measurements

A rheometer (Anton Paar RHEOPLUS/32 V3.40, USA), equipped with a plate-plate geometry of 50 mm, was used to evaluate the effect of temperature on complex viscosity, storage modulus (G′), and loss modulus (G″) of inks. A temperature sweep was performed from 40 to 4 °C at a constant frequency and amplitude gamma of 1 Hz and 0.1%, respectively. The gap size between the plate and the hydrogel was set at 0.5 mm. Each sample was initially deposited on the plate at 40 °C for 1 min to equilibrate its temperature prior to starting the measurement. In addition, a shear rate sweep and a strain sweep were conducted in the range of 0.1–100 Hz at 30 °C. All rheological measurements were conducted in triplicate.

2.5. Preparation of bioink

We prepared a blend of GelMA and alginate (Sigma-Aldrich, St. Louis, MO, USA) as follows: 1% alginate was dissolved in DPBS, and 3% (w/v) GelMA and 0.067% LAP were added to the solution. This blend was heated at 70 °C for 15 min, sterilized by passage through a 0.22 μm syringe filter (Corning®), and then let stand in a water bath at 37 °C for C2C12 cell incorporation. Separately, another ink composed of 2% (w/v) alginate in DPBS was sterilized by filtration. Both inks were then coextruded through a KSM printhead. Inks were maintained at 37 °C until the printing process was performed.

2.6. Bioprinting system setup

The inks were deposited in syringes and connected through sterile hoses to a KSM printhead equipped with three KSM elements. Syringes were placed on a syringe pump and coextruded at a flow rate of 1.5 mL/min until they reached the tip. Importantly, the nozzle outlet must be pointing upward until the inks completely fill the printhead to avoid bubble formation. The nozzle outlet was then carefully immersed in 2% $CaCl_2$ solution. When the extruded bioinks came in contact with 2% $CaCl_2$ solution at ~8 °C, alginate was immediately crosslinked, resulting in a homogeneous filament with conserved inner layered microstructures. The extrusion flow rate of 1.5 mL/min was based on preliminary experiments.

The printed constructs were subsequently deposited in a Petri dish containing sterile DPBS to allow photo-crosslinking of the GelMA using UV light at 365 nm for 30 s. Muscle constructs were cultured in ultra-low attachment 6-well plates, each one containing 3 mL of DMEM/high glucose and supplemented with 10% FBS and 1% penicillin-streptomycin.

2.7. Computational simulations

Computational fluid dynamics simulations were conducted using ANSYS Fluent 2020 Software. A multiphase model was implemented to mimic the coextrusion of fluids through a KSM printhead. A viscosity ratio of 1:1 (0.2 Pa s) and a density of 1000 kg m^{-3} were considered. A constant surface tension coefficient was added to model the interaction forces between the fluids. Tridimensional conformations were discretized by means of a mesh of triangular elements and a convergence of results was ensured using a mesh refinement. The Navier-Stokes equations for a laminar flow were also solved in a transient state. No-slip boundary conditions were imposed in the fluid-flow simulations.

2.8. Determination of cell viability

The viability of the cells in printed constructs was assessed at days 1, 7, and 28. Cross-sectional cuts were washed three times with PBS and assayed using a Live/Dead Cell imaging kit (Invitrogen, Carlsbad, CA, USA) containing 2 mM calcein AM and 4 mM ethidium homodimer (EtHD1). The samples were placed in a dark humidified incubator at room temperature for 1 h. They were then washed with PBS and immediately imaged using an Axio Observer.Z1 microscope (Zeiss, Germany) equipped with Colibri.2 LED illumination and an Apotome.2 system (Zeiss). The Apotome.2 consists in a system of moving grids coupled with an image analysis algorithm that removes out-of-focus fluorescent signals. Briefly, the system captures a set of images of a particular field-of-view at different grid-position. The image analysis algorithm filters the out-of-focus fluorescence and only displays the fluorescence signals in the plane with the sharpest focus. Every micrograph in the viability assays was taken with a 10X objective. The intensity of the LED illuminator and exposure time were 30% and 50 ms for FITC channel, and 60% and 800 ms for EtHD1 channel, respectively. Wide-field images were obtained using the stitching algorithm included in the microscope software (Zen Blue Edition, Zeiss). Viability was expressed as the ratio of viable cells over the total cell number and was derived from at least three independent constructs (n = 3).

2.9. Determination of thickness and area of layers

The layer thickness in the scaffolds printed with three, four, or six KSM elements was assessed by drawing 12 straight lines from top to bottom on cross-sectional micrographs, in orthogonal orientation to the layers. Using the line selection tool in the Fiji software (ImageJ), we measured the distance of each segment of line generated when a drawn

line was cut by each layer in the cross-section. The striation thickness distribution was expressed as the cumulative frequency of the lengths of the line segments. We also used the freehand selection tool in the Fiji software to quantify the area of single layers in cross-sectional cuts. The results were expressed as the mean of three (n = 3) independent micrographs ± standard deviation.

2.10. Analysis of cell morphology

Constructs were washed with PBS, fixed with 4% paraformaldehyde for 20 min, and washed three times with PBS to remove reagent traces. The actin filaments and nuclei were stained using Phalloidin-iFluor 647 reagent (10 µL/990 µL; ab176759, Abcam, USA) and 4′,6-diamidino-2-phenylindole (DAPI) (1 µg/mL; D9542, Sigma-Aldrich, USA), respectively. Samples were incubated with reagents in a dark humidified incubator at room temperature for 90 min, followed by three washes with PBS. The constructs were visualized using an Axio Observer.Z1 microscope (Zeiss, Germany).

2.11. Immunostaining assays

Printed constructs were washed three times with PBS and immersed in 4% paraformaldehyde for cell fixation at room temperature for 20 min. After three washes with PBS, the cells were permeabilized with Triton X-100 (0.2% v/v) for 30 min. The non-specific adhesion sites in the samples were then blocked using bovine serum albumin (1% w/v) in PBS for 30 min. The constructs were then separately treated with anti-sarcomeric α-actinin (1:200; sc-58670, Santa Cruz Biotechnology Inc., CA, USA) or anti-MYH2 (1:200; sc-53095, Santa Cruz Biotechnology, Inc., CA, USA) primary antibodies, and incubated overnight at 4 °C. The next day, the constructs were given three 5 min washes with PBS and incubated with either goat anti-mouse IgM mu chain conjugated with Alexa Fluor 647 (1:1000; ab150123, Abcam, USA), or donkey anti-mouse IgG H&L conjugated with Alexa Fluor 594 (1:500; ab150108, Abcam, USA), in a dark humidified incubator at room temperature for 1 h. The cell nuclei were then counterstained with 1 µg/mL DAPI. Fluorescence images were captured using an Axio Observer.Z1 microscope (Zeiss, Germany) in the Z-stacking mode. Reconstructed micrographs from wide-field and Z-stacked images were obtained using the microscope software (Zen Blue Edition, Zeiss).

2.12. Quantitative determination of cell orientation

We estimated the degree of orientation of muscle cells and myofibrils using Fiji software (ImageJ). Briefly, the threshold and noise in the micrographs were adjusted to allow analysis only of the sections of interest. We used the directionality tool to compute the degree of orientation of the samples based on Fourier components, at 37 bins per scalar and a histogram ranging from −90° to 90°. The frequency of the resultant values was tabulated to create a polar histogram using a custom-made algorithm in MATLAB software.

2.13. Scanning electron microscopy

A scanning electron microscope (SEM) EVO/MA25 (Zeiss, Oberkochen, Germany) with variable pressure was used to observe cross sections and axial sections of printed C2C12-laden constructs. The constructs were washed three times with PBS to remove culture media traces and then immersed in 4% formaldehyde, followed by 4% paraformaldehyde, for 15 min each. After washing again with PBS, they were passed through a graded ethanol series (25, 50, 75, and 95% EtOH for 1 h each) and then placed in a desiccator. The constructs were coated with gold and visualized by SEM at high vacuum mode.

2.14. Statistical analyses

Data were analyzed by one-way ANOVA using GraphPad Prism 8, the Welch ANOVA test, and unpaired *t*-test with Welch's correction for multiple comparisons. Significant differences between means were denoted as follows: * p-value < 0.05, ** p-value < 0.01, or *** p-value < 0.001.

3. Results and discussion

In the present study, we demonstrate the use of chaotic advection to fabricate aligned and mature muscle tissue. Our straightforward biofabrication approach only requires two hydrogel-based inks, a syringe pump, and a KSM printhead (Fig. 1B and C).

3.1. Bioprinting strategy

In continuous chaotic bioprinting, the geometry of the printhead defines the microstructure of the printed fiber. For this application, we used a printhead containing a KSM, which is a sequential array of helicoidal mixing elements that induce a spatial–periodic deformation of two or more bioinks to generate an internal layered microstructure within the printed filament (Fig. 1C I). The resultant number of lamellae or layers can be calculated according to the model $s = 2^n$, where s is the number of layers and n is the number of KSM elements in the printhead (Fig. 1C II) [27]. Therefore, printing resolution is no longer dictated by the outlet diameter of the nozzle, but instead by the number of KSM elements used.

Continuous chaotic printing generates layered structures by mixing these two hydrogel inks in a laminar flow regime [27,30]. An appropriate combination of inks is indispensable for successful generation of structures; the inks must be compatible in terms of rheology, density, polarity, and interfacial tension [28,29]. Rheology is entangled with various printing conditions, such as temperature and flow rates. Therefore, the selection of these variables is key to the success of chaotic bioprinting. We conducted a rheology analysis of a portfolio of hydrogels to identify a combination of inks with matching working properties and appropriate printing temperatures (Fig. S1, Fig. S2, and Table S1; Supporting Information). Based on this analysis, we bioprinted our muscle-like-tissue constructs by coextruding a C2C12-laden ink composed of 3% GelMA and 1% alginate, along with a 2% pristine alginate ink, at a temperature between 30 and 37 °C (Fig. S3; Supporting Information).

In addition, the combination of hydrogels was chosen based on key functional attributes. GelMA is a cell-responsive hydrogel because it preserves the cell-anchoring RGD-moieties from its collagen origin and thereby recapitulates fundamental functions of the extracellular matrix [32,33]. Alginate was used to improve both the extrudability of our hydrogel blend and the mechanical stability of the resultant scaffold. Importantly, alginate is not a cell-responsive matrix, so it provides physical barriers within the construct that hinder cell migration between layers and promote cell alignment within confined layers [34,35]. We hypothesized that the presence of inner physical barriers in chaotically printed filaments could help to align myogenic precursor cells, thereby creating a muscle fascicle at each cell-laden layer. Alginate hydrogels may not be the best option for clinical translation; however, we foresee that our technology can be adapted for its use with other materials. For instance, the adaptation of a supporting bath that receives the extruded filament would increase the portfolio of useable bioinks. Also, combinations of materials proven successful for coaxially extrude hydrogel filaments, should be easily adaptable to our system [36–38].

Both inks (C2C12-GelMA-alginate and pristine-alginate) were coextruded simultaneously at 1.5 mL/min into a 2% $CaCl_2$ bath (the crosslinking agent for alginate) using a printhead equipped with three KSM elements (Fig. 1B I). This concentration of $CaCl_2$ was chosen based on previous reports showing that concentrations below 3% are not harmful to mammalian cells [20,39–41]. The GelMA was subsequently exposed to UV light (365 nm, 950 µW cm^{-2} power at 7 cm distance from the UV light

source) for 30 s. This time was suitable for crosslinking methacryloyl groups in GelMA, as well as sufficiently short to preserve appropriate cell viability [20,39–41]. Extrusion yielded a homogeneous filament that exhibits eight inner intercalated micro-layers (Fig. 1B II-IV) of the cell-laden GelMA and pristine alginate.

Fig. 1B III-IV shows a cross-section and axial views of a printed construct with intercalated parallel layers of C2C12-GelMA-alginate and pristine-alginate layers. This spatial organization resembles the key structural features of the muscle fascicle illustrated in Fig. 1A. Fig. 1B IV also presents a post-printing Live/Dead staining confirming that a high proportion of C2C12 cells in the construct were viable after the extrusion and crosslinking processes.

3.2. Characterization of chaotically bioprinted constructs

Fig. 2A shows the cross section of chaotically printed constructs at different culture times, confirming that C2C12 cells were spatially organized in intercalated layers. Our straightforward biofabrication approach enables long-term viability, as confirmed by Live/Dead assays. A high post-printing viability was observed (86% ± 10%; Fig. 2B),

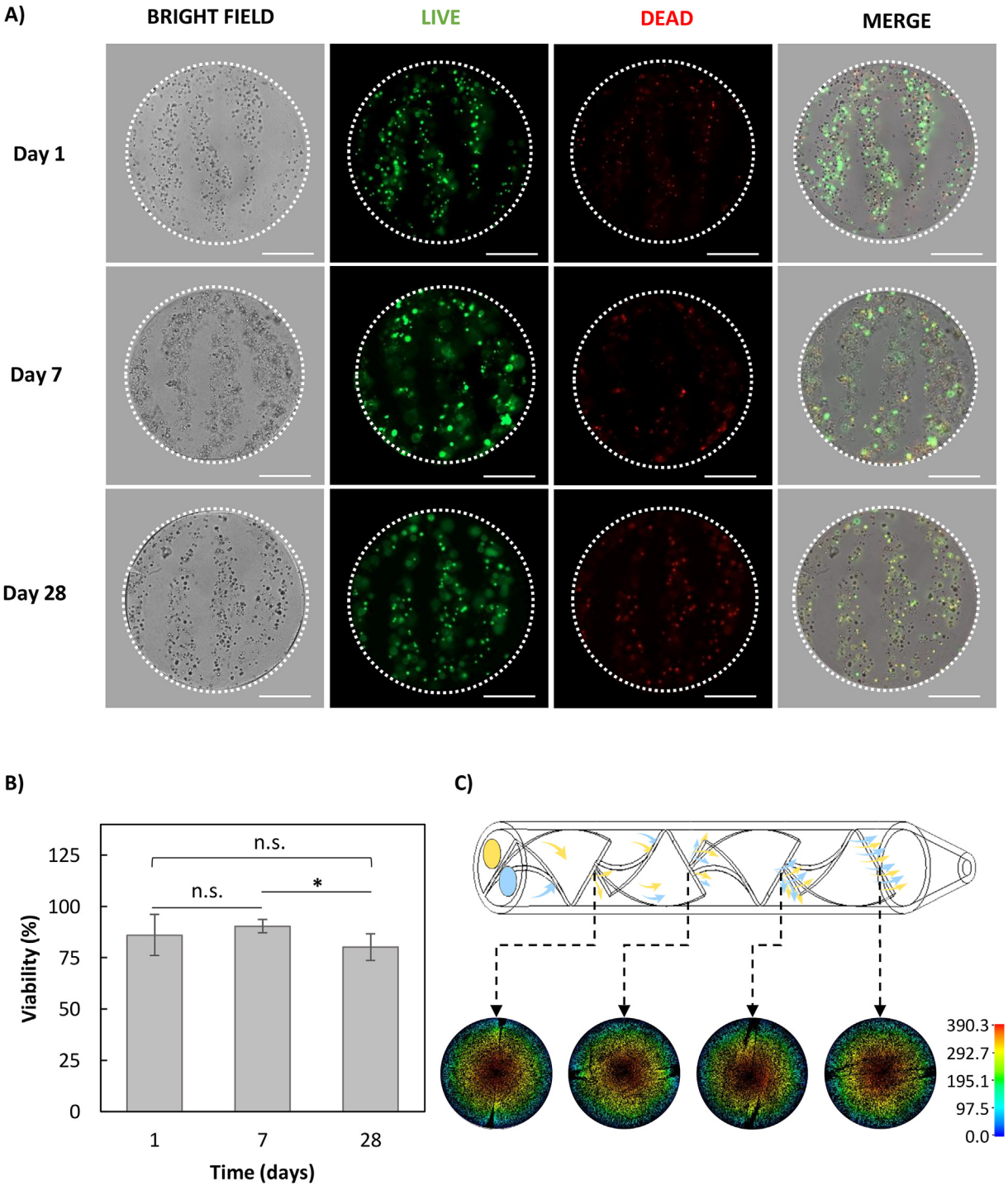

Fig. 2. Cell viability in chaotically printed constructs. A) Cross-sectional views showing bright-field and Live/Dead staining micrographs at days 1, 7, and 28. Most of cells survived the bioprinting process (Scale bar: 500 μm). **B)** Quantification of cell viability at days 1, 7, and 28 (n = 5) (*p < 0.05; n.s.: non-significant differences). **C)** Velocity profiles of the streamlines that compose the related multilayered cross-section in an extrusion process through a KSM printhead.

presumably due to the laminar flow regime that was maintained during coextrusion of the inks that minimized the shear stress on the cells [27]. A significant increase in cell viability (90% ± 3%) was noted at day 7 of cultivation (p-value ≤ 0.01), and high viabilities were observed (80 ± 7%) at day 28.

Conventional extrusion bioprinters demand a decrease in the nozzle outlet diameter to improve printing resolution, but this reduction negatively impacts cell viability (<78% for C2C12 constructs) due to the increase in shear stress at the outlet [21,26,42,43]. In chaotic bioprinting, the resolution is dictated by the number of KSM elements in the printhead, so relatively large nozzle outlets (*i.e.*, 1–2 mm) can be used [27]. For instance, the effective layer thickness is ~130 μm in constructs printed using three KSM elements with a 1 mm tip outlet (Fig. S4). This resolution can be further pushed to ~87 μm or even 22 μm when using four or six KSM elements, respectively, without any need to reduce the nozzle diameter, and with no increase in the mechanical shear stress induced by the flow, since the velocity field is not altered when the number of elements is increased [28]. Indeed, our computational simulations demonstrate that the distribution of velocity profiles after each KSM element is quite similar, with a mean value of 3912 ± 6 mm s^{-1} at the fastest region (red zone) (Fig. 2C).

3.3. Cell spreading and alignment

Our choice of hydrogels was effective in preserving the desired multilayered structure. Figs. 3 and 4 show that C2C12 cells did not migrate to neighboring layers during the time of investigation. These results confirm that the intercalated layers containing only alginate can effectively serve as physical barriers at the microscale and confine cells to the striation in which they were initially seeded. Scanning electron microscope images show this conservation of the cell-laden striation patterns over time (Fig. 3).

Continuous-chaotic bioprinting enables the facile fabrication of multiple micro-barriers (i.e., RGD-free alginate layers) in a 3D filament in a one-step protocol. Moreover, chaotic bioprinting concomitantly offers an unprecedentedly high throughput (>1.0 m min^{-1} of printed construct) [27] when compared with state-of-the-art bioprinting extrusion technologies that operate at far lower linear speeds (~0.40 m min^{-1}) [44].

Fig. 4 also shows bright-field (Fig. 4A) and fluorescence micrographs (Fig. 4B) of cell-laden constructs at different culture times with a well-preserved multilayered structure. Staining of F-actin (red) and nuclei (blue) showed that C2C12 cells started to elongate as early as day 1 after extrusion. As the culture time progressed, the elongated cells spontaneously fused with each other, as observed on day 14 (Fig. S5). Cell spreading was extensive by day 18 in the GelMA-containing layers (Fig. 4A II, 4B II), and Live/Dead assays confirmed that most of these cells were still alive at day 28 (Fig. 2A and B).

Importantly, we also observed that the elongation and spreading processes mainly occurred in cells positioned near the construct surface

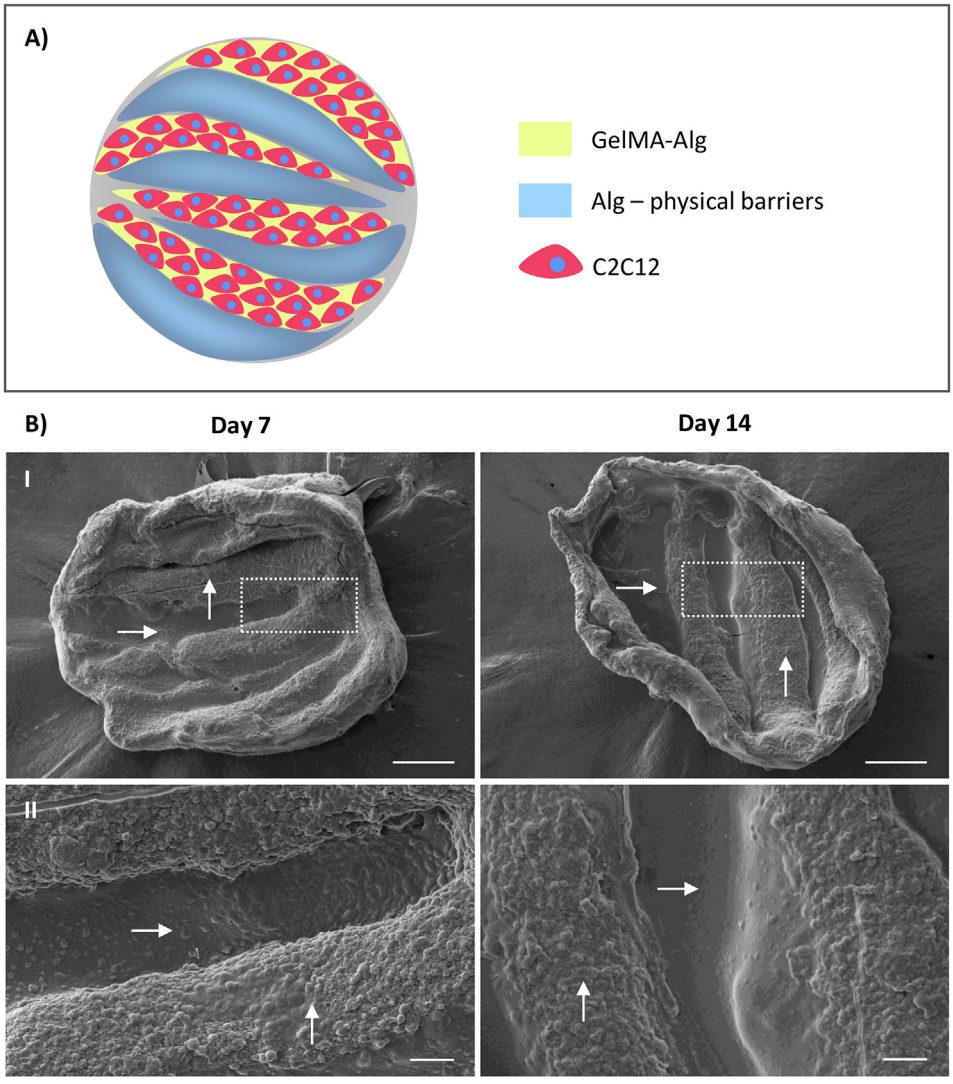

Fig. 3. Preservation of the bioprinted multilayered structure. A) Schematic representation of the internal microarchitecture in the cross-section of a bioprinted filament. B) Scanning electron micrographs of dehydrated construct-slices showing preserved cell patterns I) at day 7 and 14 (scale bar: 100 μm). (II) Magnification of the same constructs (scale bar: 10 μm). Vertical arrows show cell-containing layers, and horizontal arrows show alginate physical barriers. The presence of interspersed alginate barriers prevented C2C12 cells from invading neighboring layers.

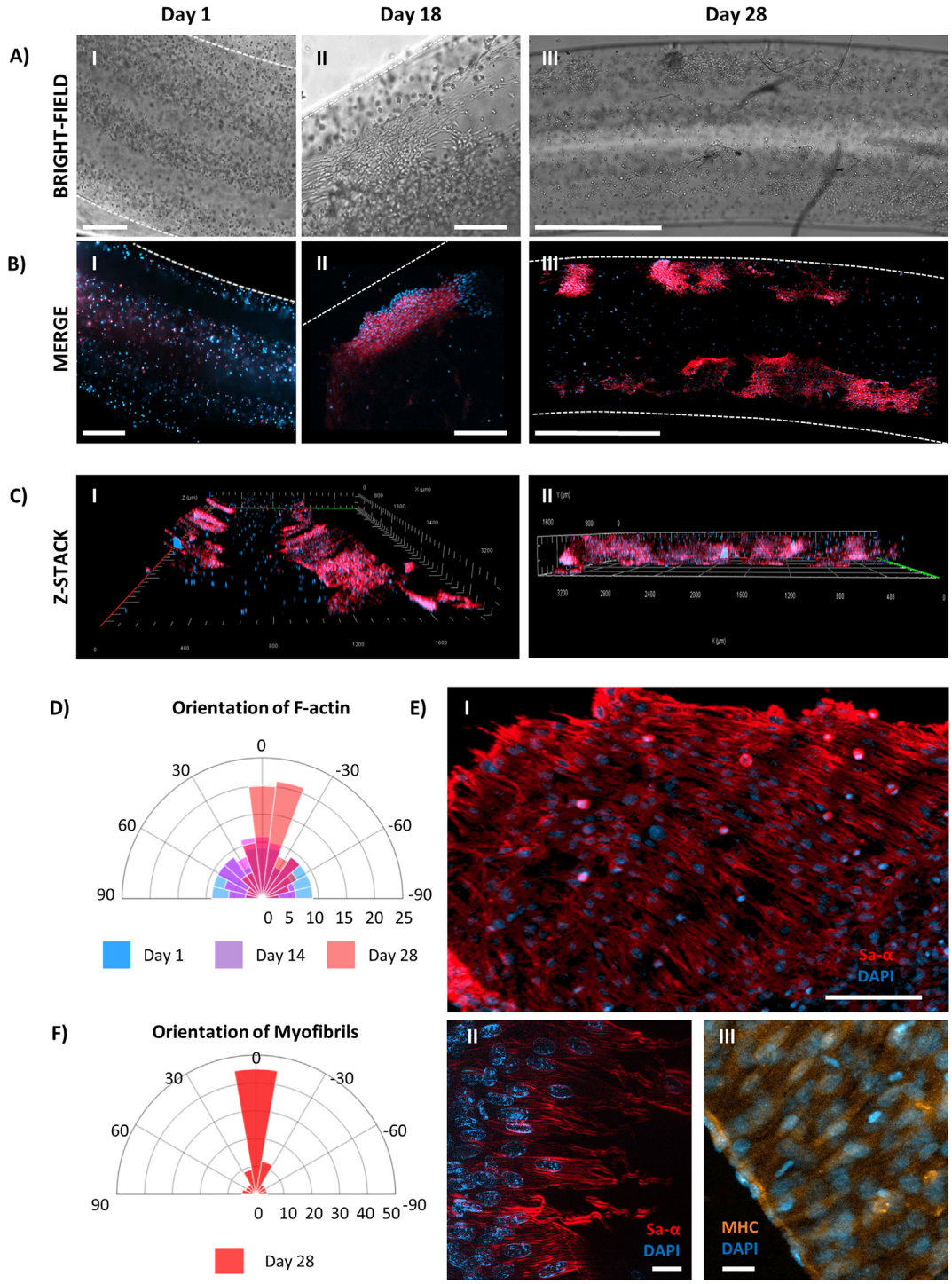

Fig. 4. Proliferation, alignment, and differentiation of C2C12 cells in chaotically printed constructs. (A) Bright-field micrographs showing the proliferation of C2C12 inside chaotically printed constructs at (I) day 1, (II) day 18 (scale bar: 200 μm), and (III) day 28 (wide-field; scale bar: 1000 μm). (B) Fluorescent micrographs of C2C12 cell striations stained with actin-DAPI [F-actin (red) and nuclei (blue)] at (I) day 1, (II) day 18 (scale bar: 200 μm), and (III) day 28 (wide-field; scale bar: 1000 μm). Cells spread and align mainly near the construct surface. **C)** Wide-field Z-stack images of a printed construct at day 28 (scale bar: 1000 μm). **(I)** Orthogonal and **(III)** axial projections showing the spreading of aligned multinucleated cells. **D)** Degree of orientation of F-actin at days 1, 14, and 28, as estimated from micrographs in panels B and C. **E)** Immunostaining of **(I)** sarcomeric α-actin (scale bar: 200 μm), and **(II)** myosin heavy chain-2 in constructs at day 28 (scale bar: 20 μm). **(III)** Myofibrils inside myotubes, surrounding cell nuclei and exhibiting a diameter of 2.1 μm at day 28 (scale bar: 20 μm). **E)** Degree of orientation of myofibrils at day 28. (For interpretation of the references to colour in this figure legend, the reader is referred to the Web version of this article.)

(Fig. 4B and C). Bright-field and Z-stack micrographs of the constructs at day 28 demonstrated that cells the steadily fused to each other and grew along the printed filament (Fig. 4B III, 4C).

The orthogonal and axial projections obtained by fluorescence microscopy also revealed that multinucleated cells spread in a direction parallel to the filament main axis (Fig. 4C I-II), thereby displaying the capacity for alignment that is required for muscle tissue functionality [11,12,45]. We calculated the degree of orientation of cells in the chaotically printed constructs with respect to the filament axis (0°) from F-actin staining micrographs using the directionality tool in Fiji software

(ImageJ; Fig. 4D). The proportion of cells aligned with respect to the filament axis (0°) increased as the culture time progressed (~30% and 58% of cells within ±25° at days 14 and 28, respectively). Previous studies have reported a similar orientation efficacy (~60%) in experiments where C2C12 cells are confined within ~150 μm thickness grooves in scaffolds [21,46].

Cell alignment is achieved by physiological processes that are both diverse and fascinating. For example, cell-cell signaling triggers collective cell migration [47]. During this coordinated behavior, the cells pull their counterparts in a specific direction, resulting in spatial orientation patterns [47,48]. Myoblasts, for example, spontaneously fuse with each other giving rise to multinucleated cells [47,49,50]. Importantly, the direction of cell alignment is greatly influenced by microscale topographies, since they impact the organization dynamics of the cytoskeleton, integrins, and focal adhesions (the protein macro-assemblies that orchestrate cytoskeleton alignment after cell attachment) [45,51]. Cell orientation is greatly determined by the spatial position at which the focal adhesions form [52], and when adhesion moieties are absent at radial directions, the focal adhesions are forced to align toward axially located cells, thereby promoting bundles of cells to adopt a specific orientation pattern [53]. Eventually, mature focal adhesions serve as the bridges by which myotubes physically connect with their surrounding counterparts [48].

The spontaneous cell alignment in our constructs is most probably a consequence of concurrent factors, namely the extrusive nature of the printing process and the chaotic bioprinting process. The result is a rapid flow alignment and the formation of parallel thin layers of cell-laden GelMA (suitable corridors for cell proliferation and elongation) separated by layers of alginate that constrain radial growth (Fig. 3).

In the case of extrusion-based bioprinting, scaffolds may exhibit anisotropic patterns that are parallel to the flow direction and these may influence cell alignment [20,21,54]. Recent work suggests that extrusion bioprinting induces muscle cells to align parallel to the extrusion direction [55,56]. The chaotic flow generated by our static mixer should induce this alignment more effectively than conventional extrusive flows. Chaotic flows exhibit an asymptotic directionality [57], and this property causes a rapid alignment of the extruded material to the intrinsic flow manifold [58,59]. In addition, the generation of intercalating layers of alginate and GelMA-alginate should further enhance cell alignment by restricting cell migration to only the GelMA-alginate layers. The use of 3% GelMA hydrogels (relatively soft) may also play synergistic roles in cellular orientation due to its facilitation of cell motility [60–62].

During alignment and maturation, multinucleated cells develop the myosin-sarcomeric actin system, a nanomachine that generates and responds to intercellular forces [50] and enables muscle contraction and movement [7,8]. These proteins are often used as targets to promote the differentiation of myoblasts into myotubes [34,63]. Our immunostaining experiment for sarcomeric α-actin (Sa-α) and myosin heavy chain-2 (MHC) identified both proteins in our cell-laden constructs at day 28 (Fig. 4E I-III). In contrast to previous studies [11,22,34,64], we did not need to use a differentiation medium to promote myotube generation; instead, we were able to use the basic culture medium recommended for myoblast cultivation, *i.e.*, Dulbecco's Modified Eagle's medium (DMEM). Other work has indicated that differentiation medium may not be required when electrical stimuli are applied to polarize myoblasts to transition to myocytes [65]. Therefore, our results suggest that the ability to induce cell differentiation is another important feature of continuous-chaotic bioprinting, since the expression of Sa-α and MHC was spontaneously influenced by the evolution of the construct.

In native muscle tissue, each myofibril is ~2 μm in diameter and is composed of sarcomeres [7]. The main constituents of sarcomeres are myosin and sarcomeric actin [8,9]. Remarkably, we observed myofibrils ~2.1 ± 0.3 μm in diameter containing nuclei and aligned to the filament axis (Fig. 4E II). In addition, these red-stained fibers exhibited high degrees of alignment, following a normal distribution (60% myofibrils within ±25° deviation) with respect to the filament axis (Fig. 4F, Supplementary Fig. S6A). In our chaotically printed constructs, the cell corridors surrounded by alginate barriers effectively aligned the myofibrils, and this alignment is a paramount factor driving the contractile capability of myotubes [22,23]. In a future contribution, we will address the effects of narrowing the layers on myofibril orientation by simply printing using more KSM elements; this narrowing is anticipated to result in even greater cellular alignment [66]. Interestingly, when skeletal muscle cells are accommodated in a confined space, the alignment patterns emerge as a result of the width of the cell corridors [15,18] and the availability of adhesion moieties [52,53] within those corridors. Narrower corridors may favor cell alignment in our multilayered constructs due to physical constraints [24,26]. However, the presence of microscale gradients of nutrients and oxygen induces cell migration to the construct surface [67], thereby working against cellular orientation along the main filament axes. In principle, narrower RGD-free physical barriers may be easier to cross in the presence of these gradients.

We also calculated the average area occupied by a single layer (1.4×10^5 μm^2) in the cross-section of constructs printed using a three-element KSM printhead (Fig. S4B, Supporting Information). Considering that the myotubes exhibited a diameter of 14.6 ± 3.1 μm at day 28 (Supplementary Fig. S6B), a single fascicle-like layer could accommodate approximately 827 myotubes. In addition, this cell diameter is within the diameter range (~10–30 μm) reported for myotubes derived from C2C12 cells [68,69]. Cell orientation might be further potentiated by successive application of physical stimuli, such as electricity, acoustic excitation, or periodic mechanical stimulation, over the printed construct [22,50,64,65,70].

Our fabrication strategy enables the bioprinting of constructs composed of fascicle-like layers resembling the hierarchical structure found in skeletal muscle tissues (Fig. 1A; Fig. 1B III). Overall, we demonstrated that continuous chaotic bioprinting is a simple-to-handle platform that offers multiple benefits, including the feasibility to biofabricate multimaterial scaffolds to unprecedented printing resolution, precise spatial accommodation of cells, mimicry of the skeletal muscle microarchitecture, high post-printing viability, alignment at both the cellular and sub-cellular levels, and differentiation of myogenic precursor cells without requiring a differentiation medium.

So far, we have demonstrated that our extrusion bioprinting method is capable of achieving hierarchically aligned architectures easily, quickly, and at a low cost. A vast number of studies have reported these structured patterns as relevant for skeletal-muscle function [34,35,71,72]. However, the functionality and maturation of our muscle-like constructs should be further demonstrated by assessing electro-conductive and contractile functions (i.e., by calcium imaging), mechanical properties (i.e., tension and compression), proteomic profiles (to assess myogenesis quality), and metabolic functions (i.e., mitochondrial activity, glucose, and lactate metabolism) [73–75].

4. Concluding remarks

The fabrication of biologically relevant tissue structures at high resolution and throughput remains a challenge in most conventional biofabrication approaches. In this contribution, we expand the use of chaotic bioprinting to the fabrication of a multilayered muscle-like tissue by continuous coextrusion of two inks of different composition throughout a printhead containing a KSM static mixer [27]. This multimaterial coextrusion was achieved by first demonstrating that effective chaotic advection can occur only with an appropriate selection of the inks and printing conditions (Fig. S2; Table S1). Specifically, we found that two hydrogels with a distinct composition should exhibit Newtonian-like behaviors at the working conditions needed for chaotic biofabrication of multilayered constructs. Coextrusion of bioinks should also be performed at a temperature range distant from T_{sg} (higher) to avoid nozzle clogging.

We further demonstrated that inner physical barriers can be incorporated into a chaotically printed construct to give rise to a structure

resembling the muscle fascicle. These barriers were generated simply by coextruding an RGD-free hydrogel (alginate) along with the myoblast-laden bioink using printheads containing three KSM elements. This strategy enabled the fabrication of ~130 μm intercalating layers containing C2C12 cells and pristine alginate. The muscle cells elongated and spontaneously aligned over time in our chaotically printed constructs, growing along the GelMA corridors and constrained by the presence of RGD-free physical barriers.

Our simple extrusion method retained a high post-printing cell viability (>86%). Remarkably, these muscle cells remained alive (>81%) even for extended periods (28 days). Our bioprinted myoblasts differentiated into myotubes expressing myosin and sarcomeric actin, the main constituents of sarcomeres. We also observed myofibrils of 2.1 μm in diameter that showed a high alignment with respect to the filament axis (60% of the myofibrils within ±25° deviation).

Overall, our results demonstrate that chaotic bioprinting is a simple and high-throughput extrusion-based printing strategy that greatly expands the portfolio of biofabrication techniques and facilitates the scalable production of tissue models. Here, we show that high-resolution microstructures can be achieved within printed filaments. Importantly, the resolution in chaotic printing is enhanced without increasing shear rate forces, thereby enabling high post-printing cell viability even at high velocity. Continuous chaotic bioprinting may offer the opportunity to study the effect of shear forces on materials and cell alignment in detail. Further, the chaotic flows the Kenics Static Mixer (and other static mixers) produces are amenable to CFD simulations (as we have shown). Therefore, the shear forces and the values of local speed can be precisely calculated at each location of this flow as well as in different operational conditions (i.e., flow rates) and geometrical configurations (i.e., different pipe diameters, numbers of elements, or types of elements).

Despite the multiple benefits of our methodology, its current version carries some limitations. For instance, the thickness of our filaments (diameter ≈ 1 mm) may be limiting the mass transfer that is essential for perfusing nutrients and gas to the full construct while effectively removing byproducts. This may explain the reduced signals of maturation at the inner region of the filament as compared to the surface. Adapting our system to concurrently extrude permanent and fugitive materials (that produce hollow channels) would overcome this limitation.

Our results also suggest that the use of chaotic flows to print multimaterial layered constructs will greatly expand the range of biofabricated tissues models. Here, we chaotically printed constructs containing adjacent layers of GelMA-alginate and pristine alginate that promoted the alignment and maturation of myogenic precursor cells. Our findings have profound implications for the fabrication of other fibrous or filamentous tissues, including cardiac muscle. We envision that chaotic bioprinting will be useful in other relevant tissue engineering scenarios that require the presence of aligned cells, adjacent micropatterning of layers containing multiple cell types, or even vasculature.

CRediT authorship contribution statement

Edna Johana Bolívar-Monsalve: Conceptualization, Methodology, Investigation, Validation, Formal analysis, Visualization, Writing - original draft. **Carlos Fernando Ceballos-González:** Conceptualization, Methodology, Investigation, Validation, Formal analysis, Visualization, Writing - original draft. **Karen Ixchel Borrayo-Montaño:** Investigation, Validation, Visualization. **Diego Alonso Quevedo-Moreno:** Software, Formal analysis, Visualization. **Juan Felipe Yee-de León:** Software, Resources. **Ali Khademhosseini:** Writing - review & editing, Funding acquisition. **Paul S. Weiss:** Writing - review & editing, Funding acquisition. **Mario Moisés Alvarez:** Conceptualization, Methodology, Writing - original draft, Writing - review & editing, Supervision, Project administration, Funding acquisition. **Grissel Trujillo-de Santiago:** Conceptualization, Methodology, Writing - original draft, Writing - review & editing, Supervision, Project administration, Funding acquisition.

Declaration of competing interest

The authors declare that they have no known competing financial interests or personal relationships that could have appeared to influence the work reported in this paper.

Acknowledgments

EJBM and CFCG gratefully acknowledge financial support granted by CONACyT (Consejo Nacional de Ciencia y Tecnología, México) in the form of Graduate Program Scholarships. GTdS, AK, and PSW acknowledge funding from the UC-MEXUS program. GTdS acknowledges funding received from CONACyT and L'Oréal-UNESCO-CONACyT-AMC (National Fellowship for Women in Science, Mexico). MMA and GTdS acknowledge funding provided by CONACyT in the form of Scholarships as members of the National System of Researchers (grant SNI 26048 and SNI 256730). AK acknowledges funding granted by the Terasaki Institute. This research has been partially funded by Tecnologico de Monterrey. We also acknowledge the primary antibodies provided by Santa Cruz Biotechnology Inc. in form of free samples. We gratefully acknowledge the experimental contributions of Brenda Giselle Flores-Garza, Sara Cristina Pedroza, Jorge Alfonso Tavares-Negrete, Ada Itzel Frías, Felipe López-Pacheco, Regina Elizabeth Vargas-Mejía, Zamantha Escobedo-Avellaneda, Brenda Guadalupe de la Cruz to this work.

Appendix A. Supplementary data

Supplementary data to this article can be found online at https://doi.org/10.1016/j.bprint.2020.e00125.

References

[1] M.K. Habibi, Y. Lu, Crack propagation in bamboo's hierarchical cellular structure, Sci. Rep. 4 (2014) 5598, https://doi.org/10.1038/srep05598.
[2] Y. Chen, X. Wang, H. Ren, H. Yin, S. Jia, Hierarchical dragonfly wing: microstructure-biomechanical behavior relations, J. Bionic Eng. 9 (2012) 185–191, https://doi.org/10.1016/S1672-6529(11)60114-5.
[3] V.C. Sundar, A.D. Yablon, J.L. Grazul, M. Ilan, J. Aizenberg, Fibre-optical features of a glass sponge, Nature 424 (2003) 899–900, https://doi.org/10.1038/424899a.
[4] L. Zhu, D. Luo, Y. Liu, Effect of the nano/microscale structure of biomaterial scaffolds on bone regeneration, Int. J. Oral Sci. 12 (2020) 1–15, https://doi.org/10.1038/s41368-020-0073-y.
[5] S.P. Magnusson, K.M. Heinemeier, M. Kjaer, Metabolic influences on risk for tendon disorders, Adv. Exp. Med. Biol. 920 (2016) 11–25, https://doi.org/10.1007/978-3-319-33943-6.
[6] R. Lozano, L. Stevens, B.C. Thompson, K.J. Gilmore, R. Gorkin, E.M. Stewart, M. in het Panhuis, M. Romero-Ortega, G.G. Wallace, 3D printing of layered brain-like structures using peptide modified gellan gum substrates, Biomaterials 67 (2015) 264–273, https://doi.org/10.1016/j.biomaterials.2015.07.022.
[7] F.H. Martini, R.B. Tallitsch, J.L. Nath, Human Anatomy, Pearson Education, 2017, https://doi.org/10.7312/luca17310-toc.
[8] J. Robert-Paganin, O. Pylypenko, C. Kikuti, H.L. Sweeney, A. Houdusse, Force generation by myosin motors: a structural perspective, Chem. Rev. 120 (2020) 5–35, https://doi.org/10.1021/acs.chemrev.9b00264.
[9] W.J. Kim, H. Lee, J.U. Lee, A. Atala, J.J. Yoo, S.J. Lee, G.H. Kim, Efficient myotube formation in 3D bioprinted tissue construct by biochemical and topographical cues, Biomaterials 230 (2020), https://doi.org/10.1016/j.biomaterials.2019.119632.
[10] J. Gilbert-Honick, S.R. Iyer, S.M. Somers, R.M. Lovering, K. Wagner, H.Q. Mao, W.L. Grayson, Engineering functional and histological regeneration of vascularized skeletal muscle, Biomaterials 164 (2018) 70–79, https://doi.org/10.1016/j.biomaterials.2018.02.006.
[11] L.T. Denes, L.A. Riley, J.R. Mijares, J.D. Arboleda, K. McKee, K.A. Esser, E.T. Wang, Culturing C2C12 myotubes on micromolded gelatin hydrogels accelerates myotube maturation, Skeletal Muscle 9 (2019), https://doi.org/10.1186/s13395-019-0203-4.
[12] M. Nakamura, T.A. Mir, K. Arai, S. Ito, T. Yoshida, S. Iwanaga, H. Kitano, C. Obara, T. Nikaido, Bioprinting with pre-cultured cellular constructs to-wards tissue engineering of hierarchical tissues, Int. J. Bioprint. 1 (2015) 39–48, https://doi.org/10.18063/IJB.2015.01.007.
[13] W. Arab, S. Rauf, O. Al-Harbi, C.A.E. Hauser, Novel ultrashort self-assembling peptide bioinks for 3D culture of muscle myoblast cells, Int. J. Bioprint. 4 (2018), https://doi.org/10.18063/IJB.v4i2.129.
[14] A.L. Baryshyan, L.J. Domigan, B. Hunt, B.A. Trimmer, D.L. Kaplan, Self-assembled insect muscle bioactuators with long term function under a range of environmental conditions, RSC Adv. 4 (2014) 39962–39968, https://doi.org/10.1039/c4ra08438a.

[15] S. Chen, T. Nakamoto, N. Kawazoe, G. Chen, Engineering multi-layered skeletal muscle tissue by using 3D microgrooved collagen scaffolds, Biomaterials 73 (2015) 23–31, https://doi.org/10.1016/j.biomaterials.2015.09.010.

[16] V. Hosseini, S. Ahadian, S. Ostrovidov, G. Camci-Unal, S. Chen, H. Kaji, M. Ramalingam, A. Khademhosseini, Engineered contractile skeletal muscle tissue on a microgrooved methacrylated gelatin substrate, Tissue Eng. 18 (2012) 2453–2465, https://doi.org/10.1089/ten.tea.2012.0181.

[17] G. Agrawal, A. Aung, S. Varghese, Skeletal muscle-on-a-chip: an in vitro model to evaluate tissue formation and injury, Lab Chip 17 (2017) 3447–3461, https://doi.org/10.1039/c7lc00512a.

[18] Y.J. Choi, T.G. Kim, J. Jeong, H.G. Yi, J.W. Park, W. Hwang, D.W. Cho, 3D cell printing of functional skeletal muscle constructs using skeletal muscle-derived bioink, Adv. Healthc. Mater. 5 (2016) 2636–2645, https://doi.org/10.1002/adhm.201600483.

[19] T.K. Merceron, M. Burt, Y.J. Seol, H.W. Kang, S.J. Lee, J.J. Yoo, A. Atala, A 3D bioprinted complex structure for engineering the muscle-tendon unit, Biofabrication 7 (2015), 035003, https://doi.org/10.1088/1758-5090/7/3/035003.

[20] M. Costantini, S. Testa, P. Mozetic, A. Barbetta, C. Fuoco, E. Fornetti, F. Tamiro, S. Bernardini, J. Jaroszewicz, W. Święszkowski, M. Trombetta, L. Castagnoli, D. Seliktar, P. Garstecki, G. Cesareni, S. Cannata, A. Rainer, C. Gargioli, Microfluidic-enhanced 3D bioprinting of aligned myoblast-laden hydrogels leads to functionally organized myofibers in vitro and in vivo, Biomaterials 131 (2017) 98–110, https://doi.org/10.1016/j.biomaterials.2017.03.026.

[21] A. García-Lizarribar, X. Fernández-Garibay, F. Velasco-Mallorquí, A.G. Castaño, J. Samitier, J. Ramon-Azcon, Composite biomaterials as long-lasting scaffolds for 3D bioprinting of highly aligned muscle tissue, Macromol. Biosci. (2018) 1800167, https://doi.org/10.1002/mabi.201800167.

[22] M. Ebrahimi, S. Ostrovidov, S. Salehi, S.B. Kim, H. Bae, A. Khademhosseini, Enhanced skeletal muscle formation on microfluidic spun gelatin methacryloyl (GelMA) fibres using surface patterning and agrin treatment, J. Tissue Eng. Regen. Med. 12 (2018) 2151–2163, https://doi.org/10.1002/term.2738.

[23] B.J. Kwee, D.J. Mooney, Biomaterials for skeletal muscle tissue engineering, Curr. Opin. Biotechnol. 47 (2017) 16–22, https://doi.org/10.1016/j.copbio.2017.05.003.

[24] A.K. Miri, I. Mirzaee, S. Hassan, S. Mesbah Oskui, D. Nieto, A. Khademhosseini, Y.S. Zhang, Effective bioprinting resolution in tissue model fabrication, Lab Chip 19 (2019) 2019–2037, https://doi.org/10.1039/c8lc01037d.

[25] F. Qian, C. Zhu, J.M. Knipe, S. Ruelas, J.K. Stolaroff, J.R. Deotte, E.B. Duoss, C.M. Spadaccini, C.A. Henard, M.T. Guarnieri, S.E. Baker, Direct writing of tunable living inks for bioprocess intensification, Nano Lett. 19 (2019) 5829–5835, https://doi.org/10.1021/acs.nanolett.9b00066.

[26] A.R. Spencer, E. Shirzaei Sani, J.R. Soucy, C.C. Corbet, A. Primbetova, R.A. Koppes, N. Annabi, Bioprinting of a cell-laden conductive hydrogel composite, ACS Appl. Mater. Interfaces 11 (2019) 30518–30533, https://doi.org/10.1021/acsami.9b07353.

[27] C. Chávez-Madero, M.D. de León-Derby, M. Samandari, C.F. Ceballos-González, E.J. Bolívar-Monsalve, C. Mendoza-Buenrostro, S. Holmberg, N.A. Garza-Flores, M.A. Almajhadi, I. González-Gamboa, J.F. Yee-de León, S.O. Martínez-Chapa, C.A. Rodríguez, H.K. Wickramasinghe, M. Madou, D. Dean, A. Khademhosseini, Y.S. Zhang, M.M. Alvarez, G. Trujillo-de Santiago, Using chaotic advection for facile high-throughput fabrication of ordered multilayer micro- and nanostructures: continuous chaotic printing, Biofabrication 12 (2020), 035023, https://doi.org/10.1088/1758-5090/ab84cc.

[28] D.M. Hobbs, M.M. Alvarez, F.J. Muzzio, Mixing in globally chaotic flows: a self-similar process, Fractals 5 (1997) 395–425, https://doi.org/10.1142/S0218348X9700036X.

[29] D.M. Hobbs, F.J. Muzzio, The Kenics static mixer: a three-dimensional chaotic flow, Chem. Eng. J. 67 (1997) 153–166, https://doi.org/10.1016/S1385-8947(97)00013-2.

[30] G. Trujillo-De Santiago, M.M. Alvarez, M. Samandari, G. Prakash, G. Chandrabhatla, P.I. Rellstab-Sánchez, B. Byambaa, P. Pour Shahid Saeed Abadi, S. Mandla, R.K. Avery, A. Vallejo-Arroyo, A. Nasajpour, N. Annabi, Y.S. Zhang, A. Khademhosseini, Chaotic printing: using chaos to fabricate densely packed micro- and nanostructures at high resolution and speed, Mater. Horizons. 5 (2018) 813–822, https://doi.org/10.1039/c8mh00344k.

[31] C.S. Russell, A. Mostafavi, J.P. Quint, A.C. Panayi, K. Baldino, T.J. Williams, J.G. Daubendiek, V. Hugo Sánchez, Z. Bonick, M. Trujillo-Miranda, S.R. Shin, O. Pourquie, S. Salehi, I. Sinha, A. Tamayol, In situ printing of adhesive hydrogel scaffolds for the treatment of skeletal muscle injuries, ACS Appl. Bio Mater. 3 (2020) 1568–1579, https://doi.org/10.1021/acsabm.9b01176.

[32] K. Yue, G. Trujillo-de Santiago, M.M. Alvarez, A. Tamayol, N. Annabi, A. Khademhosseini, Synthesis, properties, and biomedical applications of gelatin methacryloyl (GelMA) hydrogels, Biomaterials 73 (2015) 254–271, https://doi.org/10.1016/j.biomaterials.2015.08.045.

[33] C. McBeth, J. Lauer, M. Ottersbach, J. Campbell, A. Sharon, A.F. Sauer, 5 6, budge, 3D bioprinting of GelMA scaffolds triggers mineral deposition by primary human osteoblasts, Biofabrication 9 (2017) 1–14.

[34] A. Fallahi, I.K. Yazdi, L. Serex, E. Lesha, N. Faramarzi, F. Tarlan, H. Avci, R. Costa-Almeida, F. Sharifi, C. Rinoldi, M.E. Gomes, S.R. Shin, A. Khademhosseini, M. Akbari, A. Tamayol, Customizable composite fibers for engineering skeletal muscle models, ACS Biomater. Sci. Eng. 6 (2020) 1112–1123, https://doi.org/10.1021/acsbiomaterials.9b00992.

[35] J.M. Lee, W.Y. Yeong, Design and printing strategies in 3D bioprinting of cell-hydrogels: a review, Adv. Healthc. Mater. 5 (2016) 2856–2865, https://doi.org/10.1002/adhm.201600435.

[36] Y. Wang, R.K. Kankala, K. Zhu, S. Bin Wang, Y.S. Zhang, A.Z. Chen, Coaxial extrusion of tubular tissue constructs using a gelatin/GelMA blend bioink, ACS Biomater. Sci. Eng. 5 (2019) 5514–5524, https://doi.org/10.1021/acsbiomaterials.9b00926.

[37] S. Hong, J.S. Kim, B. Jung, C. Won, C. Hwang, Coaxial bioprinting of cell-laden vascular constructs using a gelatin-tyramine bioink, Biomater. Sci. 7 (2019) 4578–4587, https://doi.org/10.1039/c8bm00618k.

[38] S.C. Millik, A.M. Dostie, D.G. Karis, P.T. Smith, M. Mckenna, N. Chan, C.D. Curtis, E. Nance, A.B. Theberge, A. Nelson, 3D printed coaxial nozzles for the extrusion of hydrogel tubes toward modeling vascular endothelium. https://doi.org/10.1088/1758-5090/ab2b4d.3D, 2020, 11, 1-20.

[39] C. Colosi, S.R. Shin, V. Manoharan, S. Massa, M. Costantini, A. Barbetta, M.R. Dokmeci, M. Dentini, A. Khademhosseini, Microfluidic bioprinting of heterogeneous 3D tissue constructs using low-viscosity bioink, Adv. Mater. 28 (2016) 677–684a, https://doi.org/10.1002/adma.201503310.

[40] W. Jia, P.S. Gungor-Ozkerim, Y.S. Zhang, K. Yue, K. Zhu, W. Liu, Q. Pi, B. Byambaa, M.R. Dokmeci, S.R. Shin, A. Khademhosseini, Direct 3D bioprinting of perfusable vascular constructs using a blend bioink, Biomaterials 106 (2016) 58–68, https://doi.org/10.1016/j.biomaterials.2016.07.038.

[41] R. Seyedmahmoud, B. Çelebi-Saltik, N. Barros, R. Nasiri, E. Banton, A. Shamloo, N. Ashammakhi, M.R. Dokmeci, S. Ahadian, Three-dimensional bioprinting of functional skeletal muscle tissue using gelatin methacryloyl-alginate bioinks, Micromachines 10 (2019), https://doi.org/10.3390/mi10100679.

[42] A. Blaeser, D.F. Duarte Campos, U. Puster, W. Richtering, M.M. Stevens, H. Fischer, Controlling shear stress in 3D bioprinting is a key factor to balance printing resolution and stem cell integrity, Adv. Healthc. Mater. 5 (2016) 326–333, https://doi.org/10.1002/adhm.201500677.

[43] A. Bandyopadhyay, V.K. Dewangan, K.Y. Vajanthri, S. Poddar, S.K. Mahto, Easy and affordable method for rapid prototyping of tissue models in vitro using three-dimensional bioprinting, Biocybern. Biomed. Eng. 38 (2018) 158–169, https://doi.org/10.1016/j.bbe.2017.12.001.

[44] W. Liu, Y.S. Zhang, M.A. Heinrich, F. De Ferrari, H.L. Jang, S.M. Bakht, M.M. Alvarez, J. Yang, Y.C. Li, G. Trujillo-de Santiago, A.K. Miri, K. Zhu, P. Khoshakhlagh, G. Prakash, H. Cheng, X. Guan, Z. Zhong, J. Ju, G.H. Zhu, X. Jin, S.R. Shin, M.R. Dokmeci, A. Khademhosseini, Rapid continuous multimaterial extrusion bioprinting, Adv. Mater. 29 (2017), https://doi.org/10.1002/adma.201604630.

[45] Y. Li, G. Huang, X. Zhang, L. Wang, Y. Du, T.J. Lu, F. Xu, Engineering cell alignment in vitro, Biotechnol. Adv. 32 (2014) 347–365, https://doi.org/10.1016/j.biotechadv.2013.11.007.

[46] H. Aubin, J.W. Nichol, C.B. Hutson, H. Bae, A.L. Sieminski, D.M. Cropek, P. Akhyari, A. Khademhosseini, Directed 3D cell alignment and elongation in microengineered hydrogels, Biomaterials 31 (2010) 6941–6951, https://doi.org/10.1016/j.biomaterials.2010.05.056.

[47] W. Du, S. Hong, G. Scapin, M. Goulard, D.I. Shah, Directed collective cell migration using three-dimensional bioprinted micropatterns on thermoresponsive surfaces for myotube formation, ACS Biomater. Sci. Eng. 5 (2019) 3935–3943, https://doi.org/10.1021/acsbiomaterials.8b01359.

[48] R. Mayor, S. Etienne-Manneville, The front and rear of collective cell migration, Nat. Rev. Mol. Cell Biol. 17 (2016) 97–109, https://doi.org/10.1038/nrm.2015.14.

[49] J. Gilbert-Honick, W. Grayson, Vascularized and innervated skeletal muscle tissue engineering, Adv. Healthc. Mater. 9 (2020) 1–27, https://doi.org/10.1002/adhm.201900626.

[50] P. Heher, B. Maleiner, J. Prüller, A.H. Teuschl, J. Kollmitzer, X. Monforte, S. Wolbank, H. Redl, D. Rünzler, C. Fuchs, A novel bioreactor for the generation of highly aligned 3D skeletal muscle-like constructs through orientation of fibrin via application of static strain, Acta Biomater. 24 (2015) 251–265, https://doi.org/10.1016/j.actbio.2015.06.033.

[51] A. Leclerc, D. Tremblay, S. Hadjiantoniou, N.V. Bukoreshtliev, J.L. Rogowski, M. Godin, A.E. Pelling, Three dimensional spatial separation of cells in response to microtopography, Biomaterials 34 (2013) 8097–8104, https://doi.org/10.1016/j.biomaterials.2013.07.047.

[52] N. Xia, C.K. Thodeti, T.P. Hunt, Q. Xu, M. Ho, G.M. Whitesides, R. Westervelt, D.E. Ingber, Directional control of cell motility through focal adhesion positioning and spatial control of Rac activation, Faseb. J. 22 (2008) 1649–1659, https://doi.org/10.1096/fj.07-090571.

[53] J.M. Dugan, R.F. Collins, J.E. Gough, S.J. Eichhorn, Oriented surfaces of adsorbed cellulose nanowhiskers promote skeletal muscle myogenesis, Acta Biomater. 9 (2013) 4707–4715, https://doi.org/10.1016/j.actbio.2012.08.050.

[54] D. Pan, R. Hufenus, Z. Qin, L. Chen, A. Gooneie, Tailored gradient morphologies and anisotropic surface patterns in polymer blends, Macromol. Mater. Eng. 304 (2019), https://doi.org/10.1002/mame.201800601.

[55] J.H. Kim, I. Kim, Y.J. Seol, I.K. Ko, J.J. Yoo, A. Atala, S.J. Lee, Neural cell integration into 3D bioprinted skeletal muscle constructs accelerates restoration of muscle function, Nat. Commun. 11 (2020) 1–12, https://doi.org/10.1038/s41467-020-14930-9.

[56] Z. Wang, S.J. Lee, H.J. Cheng, J.J. Yoo, A. Atala, 3D bioprinted functional and contractile cardiac tissue constructs, Acta Biomater. 70 (2018) 48–56, https://doi.org/10.1016/j.actbio.2018.02.007.

[57] M. Giona, A. Adrover, F.J. Muzzio, S. Cerbelli, M.M. Alvarez, The geometry of mixing in time-periodic chaotic flows. I. Asymptotic directionality in physically realizable flows and global invariant properties, Phys. Nonlinear Phenom. 132 (1999) 298–324, https://doi.org/10.1016/S0167-2789(99)00018-4.

[58] M.M. Alvarez, F.J. Muzzio, S. Cerbelli, A. Adrover, M. Giona, Self-similar spatiotemporal structure of intermaterial boundaries in chaotic flows, Phys. Rev. Lett. 81 (1998) 3395, https://doi.org/10.1103/PhysRevLett.81.3395.

[59] F.J. Muzzio, M.M. Alvarez, S. Cerbelli, Massimiliano Giona, A. Adrover, The intermaterial area density generated by time- and spatially periodic 2D chaotic flows, Chem. Eng. Sci. 55 (2000) 1497–1508, https://doi.org/10.1016/S0009-2509(99)00359-0.
[60] J. Yin, M. Yan, Y. Wang, J. Fu, H. Suo, 3D bioprinting of low-concentration cell-laden gelatin methacrylate (GelMA) bioinks with a two-step cross-linking strategy, ACS Appl. Mater. Interfaces 10 (2018) 6849–6857, https://doi.org/10.1021/acsami.7b16059.
[61] W. Liu, Z. Zhong, N. Hu, Y. Zhou, L. Maggio, A.K. Miri, A. Fragasso, X. Jin, A. Khademhosseini, Y.S. Zhang, Coaxial extrusion bioprinting of 3D microfibrous constructs with cell-favorable gelatin methacryloyl microenvironments, Biofabrication 10 (2018), https://doi.org/10.1088/1758-5090/aa9d44.
[62] W. Liu, M.A. Heinrich, Y. Zhou, A. Akpek, N. Hu, X. Liu, X. Guan, Z. Zhong, X. Jin, A. Khademhosseini, Y.S. Zhang, Extrusion bioprinting of shear-thinning gelatin methacryloyl bioinks, Adv. Healthc. Mater. 6 (2017), https://doi.org/10.1002/adhm.201601451.
[63] P. Mozetic, S.M. Giannitelli, M. Gori, M. Trombetta, A. Rainer, Engineering muscle cell alignment through 3D bioprinting, J. Biomed. Mater. Res. 105 (2017) 2582–2588, https://doi.org/10.1002/jbm.a.36117.
[64] Y. Sriphutkiat, S. Kasetsirikul, D. Ketpun, Y. Zhou, Cell alignment and accumulation using acoustic nozzle for bioprinting, Sci. Rep. 9 (2019), https://doi.org/10.1038/s41598-019-54330-8.
[65] G.M. Fortunato, C. De Maria, D. Eglin, T. Serra, G. Vozzi, An ink-jet printed electrical stimulation platform for muscle tissue regeneration, Bioprinting 11 (2018), https://doi.org/10.1016/j.bprint.2018.e00035.
[66] L. Wang, Y. Wu, B. Guo, P.X. Ma, Nanofiber yarn/hydrogel core-shell scaffolds mimicking native skeletal muscle tissue for guiding 3D myoblast alignment, elongation, and differentiation, ACS Nano 9 (2015) 9167–9179, https://doi.org/10.1021/acsnano.5b03644.
[67] R. D, A.R. B, Thomas Distler, Aditya Solisito, Dominik Schneidereit, Oliver Friedrich, 3D printed oxidized alginate-gelatin bioink provides guidance for C2C12 muscle precursor cell orientation and differentiation via shear stress during bioprinting, Biofabrication 12 (2020), 0445005, https://doi.org/10.1088/1758-5090/ab98e4.
[68] E. Archer-Lahlou, C. Lan, R.T. Jagoe, Physiological culture conditions alter myotube morphology and responses to atrophy treatments: implications for in vitro research on muscle wasting, Phys. Rep. 6 (2018) 1–14, https://doi.org/10.14814/phy2.13726.
[69] S.K. Hsieh, H.Y. Lin, C.J. Chen, C.F. Jhuo, K.Y. Liao, W.Y. Chen, J.T.C. Tzen, Promotion of myotube differentiation and attenuation of muscle atrophy in murine C2C12 myoblast cells treated with teaghrelin, Chem. Biol. Interact. 315 (2020) 108893, https://doi.org/10.1016/j.cbi.2019.108893.
[70] C. Rinoldi, A. Fallahi, I.K. Yazdi, J. Campos Paras, E. Kijeńska-Gawrońska, G. Trujillo-De Santiago, A. Tuoheti, D. Demarchi, N. Annabi, A. Khademhosseini, W. Swieszkowski, A. Tamayol, Mechanical and biochemical stimulation of 3D multilayered scaffolds for tendon tissue engineering, ACS Biomater. Sci. Eng. 5 (2019) 2953–2964, https://doi.org/10.1021/acsbiomaterials.8b01647.
[71] A.C. Fonseca, F.P.W. Melchels, M.J.S. Ferreira, S.R. Moxon, G. Potjewyd, T.R. Dargaville, S.J. Kimber, M. Domingos, Emulating human tissues and organs: a bioprinting perspective toward personalized medicine, Chem. Rev. 120 (2020) 11128–11174, https://doi.org/10.1021/acs.chemrev.0c00342.
[72] S.L. Hume, S.M. Hoyt, J.S. Walker, B.V. Sridhar, J.F. Ashley, C.N. Bowman, S.J. Bryant, Alignment of multi-layered muscle cells within three-dimensional hydrogel macrochannels, Acta Biomater. 8 (2012) 2193–2202, https://doi.org/10.1016/j.actbio.2012.02.001.
[73] A.M. Jorgensen, J.J. Yoo, A. Atala, Solid organ bioprinting: strategies to achieve organ function, Chem. Rev. 120 (2020) 11093–11127, https://doi.org/10.1021/acs.chemrev.0c00145.
[74] R. Levato, T. Jungst, R.G. Scheuring, T. Blunk, J. Groll, J. Malda, From shape to function: the next step in bioprinting, Adv. Mater. 32 (2020), https://doi.org/10.1002/adma.201906423.
[75] S. Murphy, P. Dowling, K. Ohlendieck, Comparative skeletal muscle proteomics using two-dimensional gel electrophoresis, Proteomes 4 (2016), https://doi.org/10.3390/proteomes4030027.